# External Magnetic Field Effects on Shape Anisotropy of TiO<sub>2</sub> Nanostructures Grown from Paramagnetic Ti(III) Precursor

Peter Tutacz<sup>1</sup>, Daniel Stadler<sup>1</sup>, Touraj Karimpour<sup>1</sup>, Tomáš Duchoň<sup>2</sup>, Stefan Cramm<sup>2</sup>, Claus Michael Schneider<sup>2</sup>, Thomas Fischer<sup>1</sup>, David N. Mueller<sup>2</sup> and Sanjay Mathur<sup>1,\*</sup>

<sup>1</sup>Institute of Inorganic Chemistry, University of Cologne, Greinstr. 6, D-50939 Cologne

<sup>2</sup>Forschungszentrum Jülich GmbH, Peter Grünberg Institute (PGI-6), D-52425 Jülich, Germany

Keywords: Titanium dioxide, magnetic field-assisted CVD, single-source precursor, Titanium alkoxide

A new Ti(III) precursor [TiCl<sub>2</sub>(O<sup>f</sup>Pr)(pyridine)<sub>3</sub>] (1) was employed in the magnetic field-assisted chemical vapor deposition (CVD) to induce external field effects on the paramagnetic metal (d<sup>1</sup>) center during film growth. Gas-phase decomposition of 1 under variable magnetic fields (0 - 0.50 T) showed pronounced shape anisotropy in as-grown TiO<sub>2</sub> films confirmed by distinct morphological patterns and preferred crystallographic orientation of the grains. The electronic structure of the Ti–O manifold derived from X-ray absorption spectroscopy showed the formation of well-defined anatase type TiO<sub>6</sub> subunits in the case of field-assisted processes (0.50 T), whereas distortions towards TiO<sub>6</sub> units of the rutile modification were seen for the zero-field experiments. The contact-less control of morphology, micro- and electronic structure of the CVD deposits through field influence offers new opportunities for *in-situ* control of material characteristics.

# 1. Introduction

Titanium dioxide (TiO<sub>2</sub>) thin films are of great significance due to their distinctive semiconductor properties, essential in optoelectronics and photocatalytic applications. Consequently, a large variety of techniques have been developed to deposit titanium oxide thin films.<sup>2-4</sup> Employing different synthesis methods in solution, such as sol-gel, hydrothermal, co-precipitation<sup>4</sup> and gasphase, such as plasma-enhanced chemical vapor deposition (PE-CVD)<sup>5</sup>, chemical vapor deposition (CVD)<sup>6</sup>, sputter deposition<sup>7</sup> or atomic layer deposition (ALD)<sup>8</sup>, phase composition and morphology evolution can be controlled. A large number of titanium (IV) compounds (e.g., TiCl<sub>4</sub>, Ti(OEt)<sub>4</sub>) are commercially available and predominantly used to produce TiO<sub>2</sub> thin films and powders used in photovoltaic cells<sup>1</sup>, photocatalysis<sup>2</sup> and gas sensors<sup>3</sup>. However, the availability of volatile titanium precursors in subvalent oxidation state (Ti<sup>3+</sup>) is scarce, given their propensity towards oxidation (Ti(III)  $\rightarrow$  Ti(IV) + e<sup>-</sup>) and thermodynamically preferred disproportionation reactions<sup>9</sup>. Nevertheless, a few examples of Ti(III) complexes, stabilized by electronic saturation of the Ti(III) center with electron-rich ligands, such as amidinates 10,11 or heterocyclic carbenes 12-<sup>14</sup>, are known. Following a similar concept, the syntheses of bimetallic Ti(III) molecules together with Al(III)<sup>15</sup>, Th(III) and U(III)<sup>16</sup> were recently reported in which electron-rich cyclopentadienyl unit (and analogous derivatives) was judiciously chosen to stabilize the trivalent metal centers. Even though this synthesis strategy successfully delivered the target Ti complexes, the resulting molecules showed very low vapor pressures limiting their applicability in chemical vapor growth processes as a volatile source or alternatively requiring carrier gases to sustain precursor feedstock in the vapor phase. In our quest for volatile Ti(III) species, we have synthesized a new set of heteroleptic compounds with trivalent titanium centers stabilized by pyridine as a neutral co-ligand, which provides reasonable air stability and volatility to these precursors, essential for CVD

experiments.<sup>17–19</sup> In addition, the covalent coordination of alkoxo ligands to Ti centers facilitates metal oxide formation at the molecular scale without the necessity of additional reactants.

The search for CVD precursors containing a subvalent titanium center was driven by the simplistic electronic configuration with only one electron in the d-subshell (d<sup>1</sup> system) that offers possibilities to study the role of paramagnetic centers during CVD in an external magnetic field (mfCVD). The significant effect of a small (< 1 T) external magnetic field has been recently demonstrated exhibiting striking changes in the morphology, phase and crystallographic orientation of d-electron-rich materials grown under field-assisted conditions.<sup>20–22</sup> For instance, anisotropic growth along field lines was observed during mfCVD of a zero-valent iron precursor (Fe(CO<sub>5</sub>)), whereas multi-facetted larger particulates with preferred surface orientation were obtained in the deposition of iron oxides from a trivalent iron precursor, [Fe(O'Bu)<sub>3</sub>]<sub>2</sub>.<sup>21</sup> These first reports demonstrated new possibilities for contactless control over microstructure and morphology during thin film growth. Herein, we report (i) mfCVD experiments in different field orientations (parallel and perpendicular to the substrate) with (ii) a rationally designed Ti<sup>3+</sup> molecular precursor to demonstrate the field influences on characteristics of the resulting material originating from a magnetically susceptible molecular precursor. The precursor configuration was confirmed by single crystal X-ray diffraction analysis that revealed a trivalent titanium center in an octahedral environment.

# 2. Results and discussion

[TiCl<sub>2</sub>(O'Pr)(py)<sub>3</sub>] (1) was synthesized by reacting a stoichiometric amount of potassium alkoxide with the pyridine adduct [TiCl<sub>3</sub>(py)<sub>3</sub>] (3) in cold toluene (Figure 1b). The excess solvent was removed under reduced pressure ( $10^{-2}$  mbar) and the as-obtained product was purified by extraction in toluene. For synthesizing [TiCl<sub>3</sub>(py)<sub>3</sub>], titanium(III) chloride was isolated as a THF-adduct

[TiCl<sub>3</sub>(THF)<sub>3</sub>] (**2**) following a published procedure, by reacting 3 equivalents of TiCl<sub>3</sub>·AlCl<sub>3</sub> in toluene with THF.<sup>14</sup> The reaction mixture was gradually heated to 70 °C followed by refluxing for 24 hours to obtain **2** as a blue powder. The crude product was washed three times with *n*-pentane and dried at 25 °C and 10<sup>-2</sup> mbar to yield a pale blue powder. Single crystals of [TiCl<sub>2</sub>(O<sup>i</sup>Pr)(py)<sub>3</sub>] were obtained by crystallization from a concentrated solution (toluene/isopropyl alcohol).

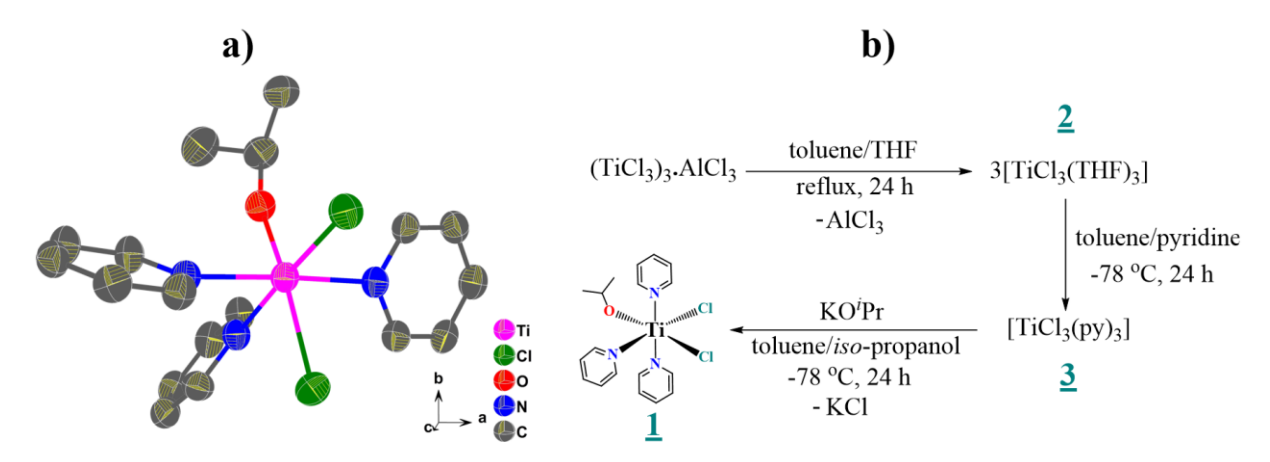


Figure 1: (a) Molecular structure of complex 1 with atoms as 50% ellipsoids, H atoms omitted for clarity, (b) synthetic pathway for complex 1.

The single crystal X-ray diffraction analysis of the titanium (III) compound revealed a monomeric complex with distorted octahedral coordination around the Ti(III) center (Fehler! Verweisquelle konnte nicht gefunden werden.a). The coordination sphere is constituted by one chloride and three neutral pyridine ligands that form the square planar coordination around the metal center, whereas the second chloride ligand binds in a *cis* symmetry with respect to the other chloride ligand. Both Ti–Cl bonds were determined as equidistant (2.4337(10) and 2.4361(10) Å), while slightly elongated bond lengths were found for the Ti–N bonds (from 2.229(3) Å and 2.237(3) Å to 2.248(3) Å). Crystal data and selected atomic distances and angles of compound (1) are summarized in Table S1 and Table S2.

The structural integrity of 1 in solution was confirmed by UV-Vis spectra (Fehler! Verweisquelle konnte nicht gefunden werden.a) exhibiting a broad and intense band with double-structured peaks centered at 445 and 515 nm, possibly due to electronic transitions from the <sup>2</sup>T<sub>2</sub> ground state of Ti<sup>3+</sup> to the <sup>2</sup>E excited state (Fehler! Verweisquelle konnte nicht gefunden werden.a). The doublet structure stems from the Jahn-Teller splitting of the <sup>2</sup>E excited state<sup>23,24</sup> and the decay of these absorptions is coupled to the oxidation of Ti<sup>3+</sup>. Hence, we were able to study the decomposition of the precursor under ambient conditions by exposing the precursor solution to air and concomitantly measuring the absorption spectra. For this purpose, 1 was dissolved in toluene and transferred to a closed quartz cuvette under inert handling conditions. The UV-Vis spectrum recorded at t = 0 min (black line in Fehler! Verweisquelle konnte nicht gefunden werden.a) marks the starting point of the experiment and showed an intact, non-oxidized Ti<sup>3+</sup> center in the precursor, as clearly visible in the absorption maxima observable at 445 nm and 515 nm. Notably, the precursor already started to decompose within minutes of air exposure, indicating high sensitivity of the molecule towards moisture and oxygen. With further progress of the experiment, a homogeneous decay of both absorption modes was evident in the gradual disappearance of the Ti<sup>3+</sup> absorption mode, which is no longer detectable after 30 minutes of air exposure.

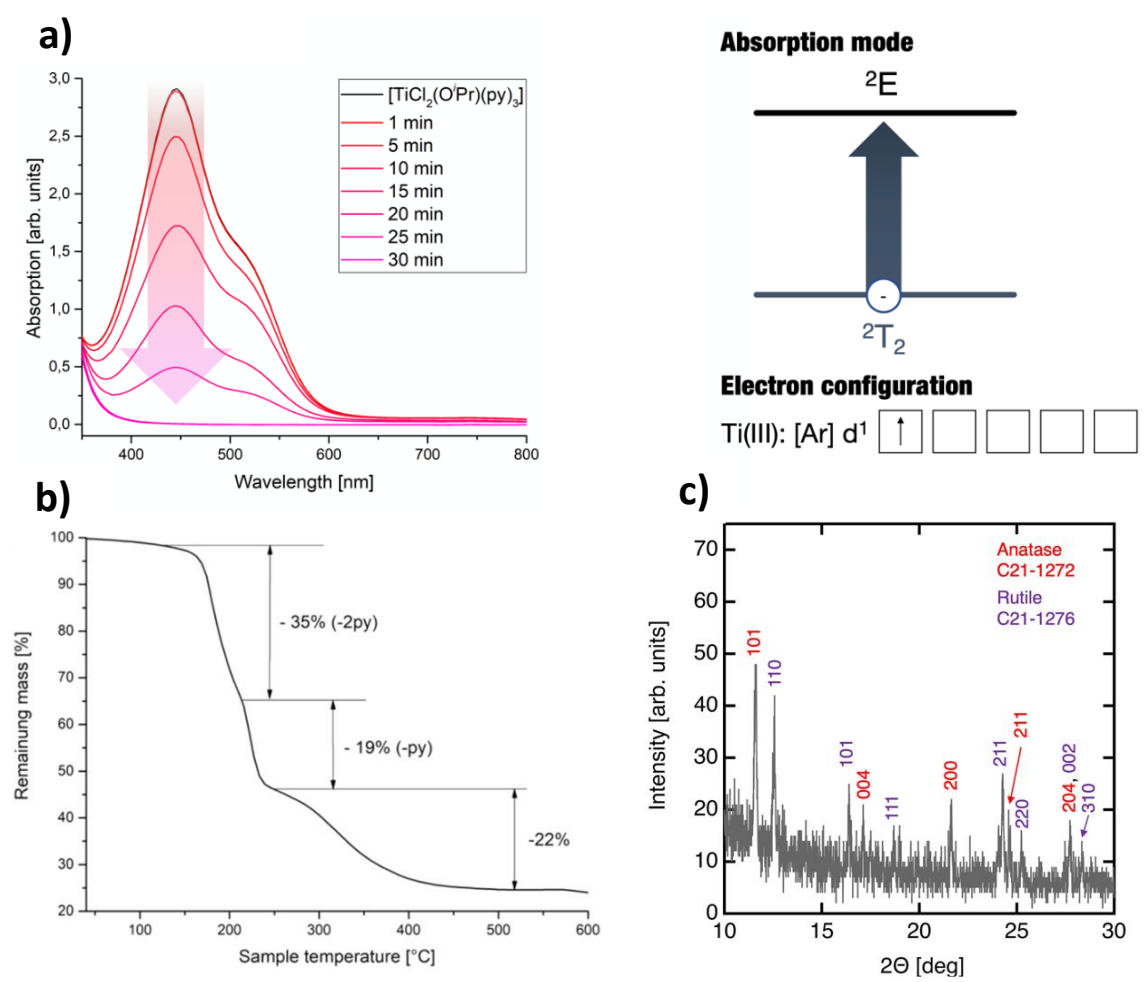


Figure 1: (a) UV-Vis spectra of [TiCl<sub>2</sub>(OiPr)(py)<sub>3</sub>] under inert and ambient conditions, with an illustration of the absorption mode and the corresponding electronic excitation; (b) TGA of [TiCl<sub>2</sub>(OiPr)(py)<sub>3</sub>] in N<sub>2</sub> atmosphere and (c) post-annealed powder powder diffraction pattern of the residue.

The volatility and thermal stability of **1** were analyzed by thermogravimetric analysis (TGA) performed under a nitrogen stream, which showed a three-step decomposition of the precursor to amorphous TiO<sub>2</sub> (**Fehler! Verweisquelle konnte nicht gefunden werden.**). The desorption of two pyridine ligands was observed at 150 °C, followed by the third pyridine ligand desorbing at 200 °C. The staggered elimination of chemically equivalent pyridine ligands suggested an intramolecular

rearrangement of ligands and geometrical constraints associated with transforming the six-fold coordination (octahedral) into a four-fold (tetrahedral) coordination in 'TiCl<sub>2</sub>(O<sup>i</sup>Pr)(py)'. The final decomposition step and formation of amorphous TiO<sub>2</sub> was achieved at 500 °C. Calcination of the residue at 1100 °C led to a mixture of rutile and anatase modifications verified by powder diffraction analysis (**Fehler! Verweisquelle konnte nicht gefunden werden.**).

The CVD experiments were performed in a customized cold wall reactor, fitted with electromagnets for applying external magnetic fields (up to 1 T) and a rotatable heater, which allowed to study the influence of magnetic field orientation on thin film growth from 1. Experiments were performed in zero-field (0.00 T,  $\alpha$  = 90°, Figure ), and with parallel (B = 0.50 T,  $\alpha$  = 0°, Figure ) and perpendicular magnetic field orientation (B = 0.50 T,  $\alpha$  = 90°, Figure ). The precursor reservoir was maintained at 120.0(3) °C, whereas the silicon substrate was kept at 600(2) °C.

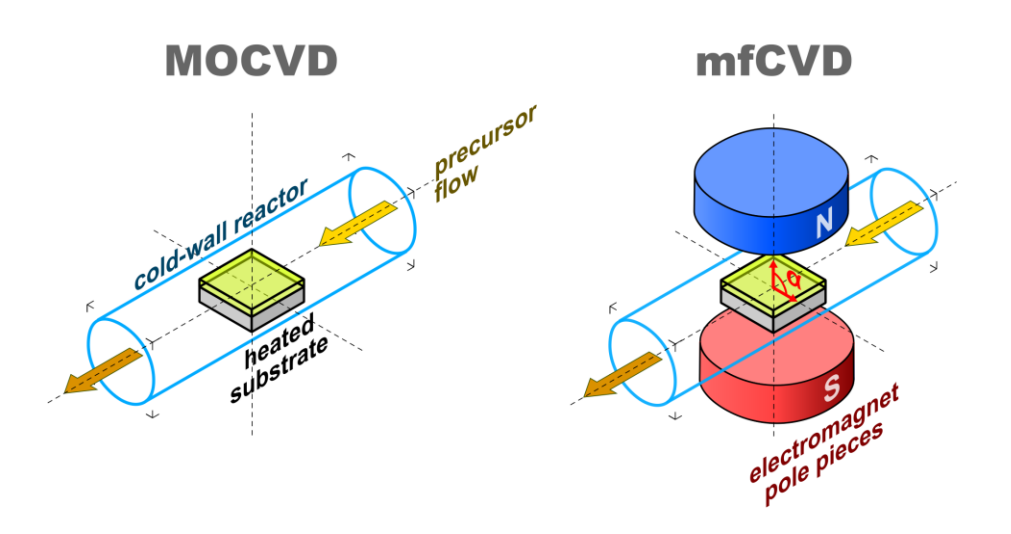


Figure 3: Schematic differences between conventional MOCVD (left) and mfCVD reactor (right). Both reactors are operated at a reduced base pressure of  $10^{-6}$  mbar. The tilting angle  $\alpha$  between the magnetic field vectors and the substrate plane is highlighted.

The X-ray diffraction (XRD) pattern showed the formation of single phase anatase for fieldassisted experiments, independent of the chosen field orientation (Figure 4), with field-related changes in relative intensities of (200) and (101) peaks (PDF: C21-1272, Figure 4). Specifically, the perpendicular field orientation led to increased intensity of the (101) peak, while parallel field orientation resulted in higher intensity of the (200) peak. The zero-field sample showed a strong peak of the (200) crystallographic plane of anatase with the coexistence of rutile, as seen in the appearance of peaks that could be indexed to the (221) and (420) planes (Figure 4, PDF C21-1276). To elaborate the interaction of the paramagnetic precursor (d<sup>1</sup> system) with the external magnetic field, the experiments were conducted under similar conditions using the diamagnetic (d<sup>0</sup> system) tetravalent Ti(O<sup>i</sup>Pr)<sub>4</sub> as the precursor molecule. In contrary to the observations made for the trivalent precursor molecule, the experiments with Ti(O<sup>i</sup>Pr)<sub>4</sub> revealed no microstructural changes for the two magnetic field orientations (Figure S1 and S2) and resulted in phase pure anatase growth. The comparison of trivalent and tetravalent Ti metal centers in the mfCVD precursor allowed us to show the importance of d-electrons for mfCVD effects on texture and morphology (vide supra). Whereas plasma enhanced chemical vapor deposition (PE-CVD) can have a reducing effect <sup>25,26</sup>, the CVD of Ti(III) precursor resulted always in the oxidized species (Ti(IV) oxide), irrespectively of the magnetic field strengths or orientation. While no changes in the crystal structure were found for the d<sup>0</sup> configuration, the d<sup>1</sup> electronic configuration seems to trigger field interactions, leading to the orientation-dependent growth directions. Since thermal treatment of the paramagnetic precursor did not result in anisotropic microstructure formation, thermal fluctuations during the process can be ruled out as the reason for the measured variation in crystal growth. Comparable texturing effects of TiO<sub>2</sub> were already described for electric field-assisted CVD<sup>27–30</sup>, as well as for the magnetic field-assisted deposition of ReN<sup>20</sup> and iron oxide<sup>22</sup>. As elaborated elsewhere<sup>22</sup>, the electric component of the field was negligible and the observed field effect can be solely attributed to the magnetic component of the field.

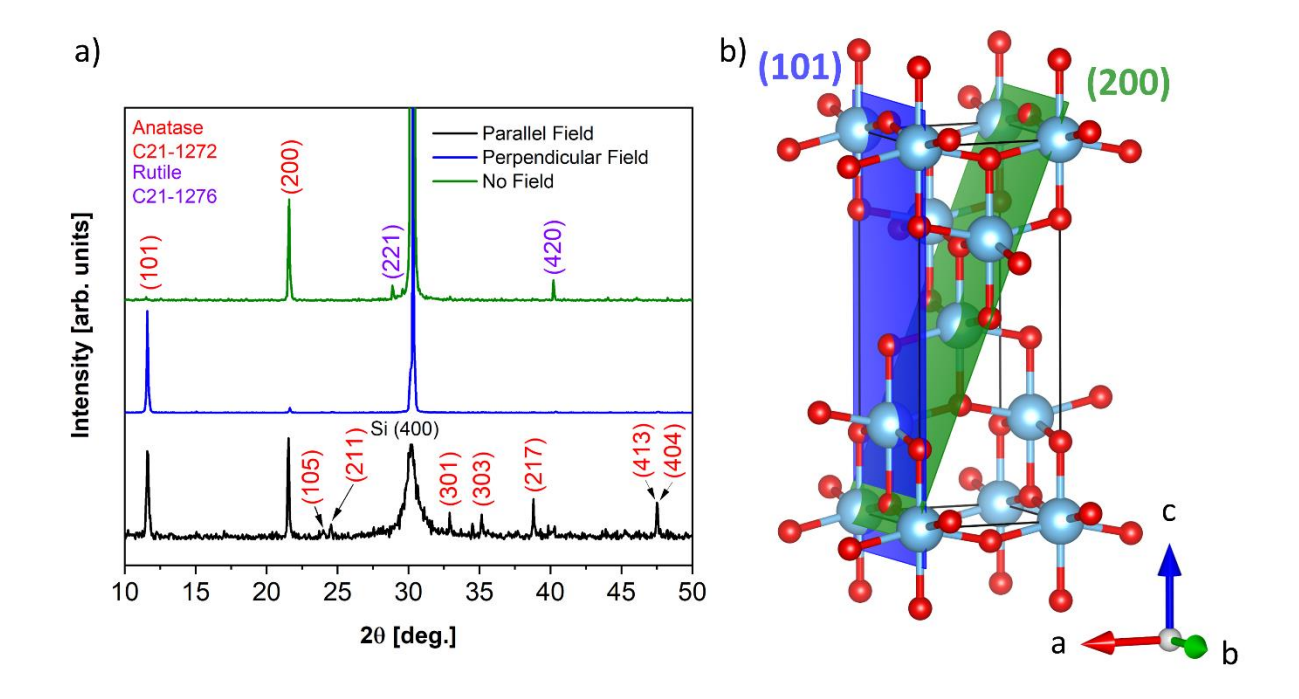


Figure 4: (a) XRD pattern of the TiO<sub>2</sub> films deposited at 600 °C; (b) the unit cell of anatase modification. The zero-field diffractogram showed traces of the rutile phase, as indexed by PDF C21-1276, whereas solely anatase (PDF C21-1272) was formed in field-assisted processes.

Besides changes in the preferred crystallographic orientation, thin films obtained from different field environments exhibited varying morphologies, as depicted in Figure 5. The zero-field deposition (Figure 5a) showed micrometer-sized flakes with smaller particulates randomly distributed over the film (red arrows), which were absent in the case of the field-assisted processes. While the films grown under the influence of parallel magnetic field ( $\alpha$ =0°, Figure 5b) exhibited continuous micrometer-sized particulates, the perpendicular magnetic field ( $\alpha$ =90°, Figure 5c) led to the formation of nanoparticles agglomerated into secondary (hierarchical) structures with flake-like morphology, but well-defined interfaces (insets in Figure 5b and c). The observed changes with magnetic field in the resulting crystal structure are in line with the obtained differences in

morphology. A comparable influence of magnetic field orientation during mfCVD of iron nanostructures was recently reported by our research group<sup>21</sup> and the results reported here expand the experimental space from systems with several d-electrons to single d-electron systems.

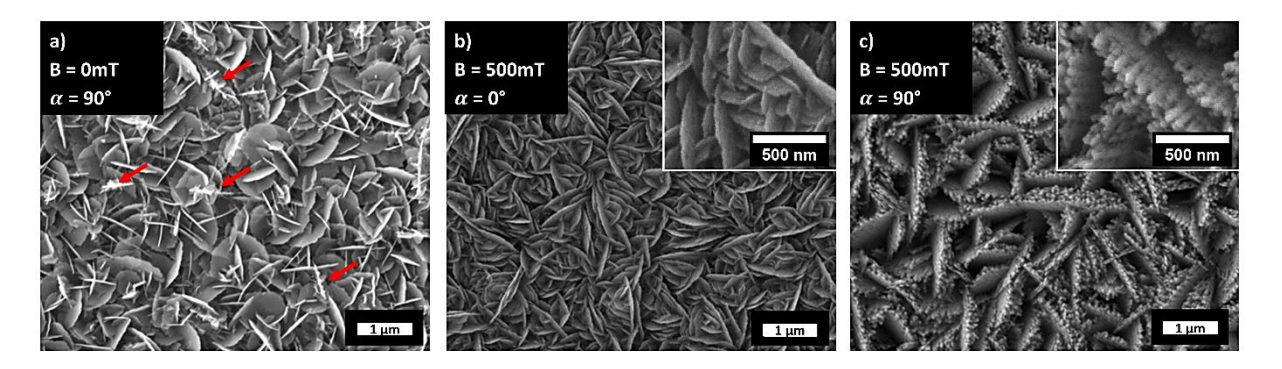
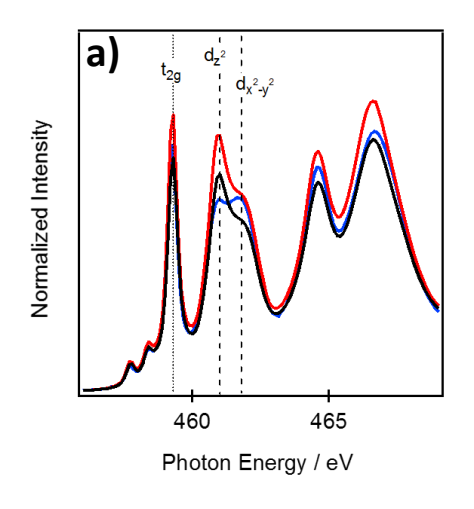


Figure 5: SEM images of TiO<sub>2</sub> films formed through mfCVD in (a) zero-field, (b) parallel and (c) perpendicular magnetic field orientation. Structural inhomogeneities are marked with red arrows. The insets demonstrate increased particulate appearance of the as-obtained films.

The experimental findings suggest that the interplay of intrinsic electronic properties (d-electron configuration) of **1** and the applied magnetic field leads to stabilization of the anatase phase with a microstructure exhibiting a strong dependence on the field orientation. Furthermore, the morphology of the films was considerably altered in different field environments. To study short range order in the TiO<sub>6</sub> subunits of the material, the effect of the magnetic field on the electronic structure of the obtained films was investigated by X-ray absorption spectroscopy (XAS) at the Ti-L<sub>3,2</sub>- and O-K-edges. The Ti-L<sub>3,2</sub>-edges of the films deposited with magnetic field assistance showed a shape characteristic for anatase<sup>31,32</sup> (Figure 6a), which is most succinct in the split  $e_g$  derived resonances around 461 eV. The characteristic splitting of the  $e_g$  into the  $d_{z2}$  and  $d_{x2-y2}$  states (marked with dashed vertical lines) and their intensity ratios stem from the distortion of the TiO<sub>6</sub> octahedra, which is different in the rutile and anatase polymorphs of TiO<sub>2</sub><sup>31</sup>. The spectrum recorded for the zero-field deposited sample, however, showed an increased  $d_{x2-y2}$  resonance, either

originating from basal distortions in the TiO<sub>6</sub> building block of the anatase structure resulting in more rutile like short-range order, or the presence of rutile impurities as found in the diffraction patterns. These findings further emphasize the magnetic field as an additional experimental parameter for phase-controlled material synthesis. The O-K-edge for the field-assisted depositions (Figure 6b) is in accordance with the reported spectroscopic signature for anatase<sup>33,34</sup>. The XAS of the zero-field deposited sample showed different behavior with the region between 540 and 550 eV exhibiting less pronounced peaks, as observed in amorphous TiO235, pointing towards the presence of distorted TiO<sub>6</sub> octahedra as already alluded by the Ti-L<sub>3,2</sub>-edges. This is coherent with studies on the CVD of iron oxide films, where the application of external magnetic-field was found to result in improved crystallinity.<sup>22</sup> A close inspection of the  $t_{2g}$  and  $e_{g}$  signals (dotted and dashed lines in Figure 6b, respectively) showed a small difference in peak height, with the intensity of t<sub>2g</sub> being reduced with respect to eg in the sample deposited in parallel field orientation. This pointed towards a slight reduction (TiO<sub>2-x</sub>) of the sample that would stabilize Ti<sup>3+</sup> centers<sup>34–36</sup>. However, the almost identical shapes of the Ti- L<sub>3,2</sub>-edges indicated that only a small amount of Ti<sup>3+</sup> is present in the sample, indicating the need for further investigation of decomposition of 1 during mfCVD.



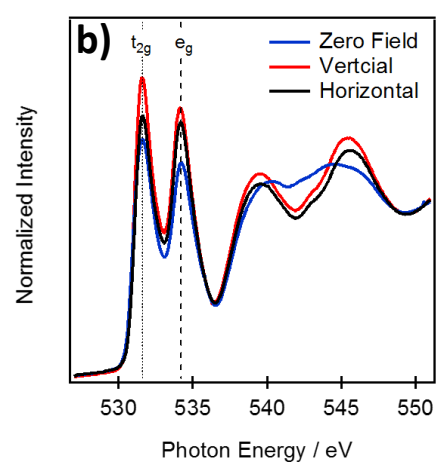


Figure 6: The X-ray absorption spectrum of the Ti-L<sub>3,2</sub>-edge (a) and O-K-edge (b) of zero-field (blue), parallel field (red) and perpendicular field (black) arrangement. The corresponding d-orbital energies are marked in the spectrum.

# 3. Conclusion

This work reports on the synthesis of a new volatile  $Ti^{3+}$  precursor  $[TiCl_2(O^iPr)(py)_3]$  (1) and its phase-selective transformation to anatase in a magnetic field-assisted CVD process. The use of magnetic fields during materials synthesis represents a new direction to fabricate self-assembled microstructures with hierarchical features and allows to tune the electronic microstates of the semiconductor films, which can be beneficial for photo- or electrocatalytic applications<sup>37</sup>, as well as provide unique surface morphologies for surface enhanced spectroscopic methods.<sup>38</sup> The results obtained with the paramagnetic Ti(III) species show strong effects of external magnetic fields on the phase composition, grain growth and crystallographic orientation altering the morphology, chemical topography and functional properties of the deposited films. For instance, a preferred growth along the <h00> crystallographic axes and formation of rutile impurities were seen for zerofield experiments, while the application of external magnetic field (0.5 T) modulated the phase evolution producing single-phase anatase films with (101) crystallographic orientation. Compared to conventional experimental parameters of chemical vapor deposition such as temperature, pressure and precursor chemistry, investigations on effects of extrinsic parameters (e.g., magnetic field) unravel new dimensions in controlling reaction pathways and in-situ alter the material properties.

# 4. Experimental section

Precursor Synthesis. All chemical syntheses and experimental manipulations were performed under inert conditions and in the absence of atmospheric moisture. For this purpose, an all-glass

Stock assembly was used for the synthesis of new compounds and intermediates. The manipulation and storage of as-synthesized samples were performed in a glovebox under argon atmosphere. Toluene, THF and *n*-pentane were dried according to standard procedures by distillation over sodium and stored over sodium wire under nitrogen atmosphere. Iso-propyl alcohol was also dried by distillation over sodium and was stored over activated 4 Å molecular sieves. Pyridine was dried by distillation over calcium hydride and stored over activated 4 Å molecular sieves.

[TiCl<sub>3</sub>(THF)<sub>3</sub>] (2). was prepared according to a procedure described by Jones et al.<sup>14</sup> Yield: 81% (18.6g), CHNS (found/calculated) [%]: C (38.92/38.90); H (6.57/6.53)

[TiCl<sub>3</sub>(py)<sub>3</sub>] (3). 25 ml of pyridine were slowly added to a stirred cold, pale blue suspension of 2 in toluene (2.0 g, 5.4 mmol, 50ml, -78°C). The mixture was allowed to warm up to room temperature over 24 hours. Shortly after mixing the reactants, the color of the reaction mixture changed to reddish-green. After 24 hours, stirring was stopped and the green powder settled down was separated by decanting the supernatant solution. The product was washed three times with 25 ml of *n*-pentane and dried under reduced pressure. Yield: 92 % (4.97 mmol, 1.94 g) CHNS (found/calculated) [%]: C (46.15/46.01); H (3.91/3.86); N (10.65/10.73)

[TiCl<sub>2</sub>(O<sup>i</sup>Pr)(py)<sub>3</sub>] (1). 30 ml of a KO<sup>i</sup>Pr solution was slowly added to a stirred cold, green solution of **3** in toluene (1.49 g, 3.8 mmol, 20 ml). For this purpose, 149 mg of potassium (3.8 mmol) was dissolved in 30 ml *iso*-propanol. The mixture was allowed to warm up to room temperature over 24 hours. After 24 hours, the brownish-red solution was dried under reduced pressure and redissolved in 100 ml toluene and stored at -28 °C to yield red crystals. Yield: 68 % (2.59 mmol, 1.08 g) CHNS (found/calculated) [%]: C (51.48/52.07); H (5.53/5.34); N (9.68/10.12). UV/VIS (toluene):  $\lambda_{\text{max}}$ : 445 nm [v = 22472 cm<sup>-1</sup>], EI-MS 70 eV: m/z (intensity) 342 (40 %) [Ti<sub>2</sub>(O<sup>i</sup>Pr)<sub>2</sub>(py)<sub>2</sub> - 2CH<sub>3</sub>]<sup>+</sup>, 267 (28 %) [Ti<sub>2</sub>(OiPr)<sub>2</sub>(py)<sub>4</sub> + 2H<sup>+</sup>]<sup>2+</sup>, [Ti(py)<sub>2</sub> + 2H<sup>+</sup>]<sup>2+</sup>, 207 (41 %) [Ti<sub>2</sub>(O<sup>i</sup>Pr)<sub>2</sub>(py)<sub>2</sub> + 2H<sup>+</sup>]<sup>2+</sup>, 79 (39 %) [py]<sup>+</sup>, 18 (100 %) [H<sub>2</sub>O]<sup>+</sup>. The crystallographic data for

# complex 1 has been submitted to the Cambridge Crystallographic Data Centre, and its corresponding CCDC number is 2284325.

CVD Experiments. Magnetic field-assisted CVD (mfCVD) experiments were performed in a horizontal cold-wall CVD reactor fitted with a silicon carbide heater, which can be rotated to adjust the desired angle between the substrate and magnetic field. The precursor was introduced to the reactor through a glass flange and evacuated to 4 x 10<sup>-5</sup> mbar. The precursor reservoir was evacuated for long periods of time before each process to limit any unwanted residual oxygen. For each process, the substrate was heated to 600°C, whereas the precursor reservoir was kept at 120 °C to achieve a homogeneous gas flow to the substrate. The film growth time was set to 45 min. for each process. After the growth, the samples were cooled to room temperature in vacuum and stored under ambient conditions.

Material Characterization. Single crystal X-ray diffraction analyses were performed on a STOE IPDS I/II diffractometer using graphite-monochromated Mo-K $\alpha$  radiation ( $\lambda$  = 0.71071 Å). SHELXS<sup>39</sup> and SIR-92<sup>40</sup> were used for the structural solution with the least square fit, using SHELXL<sup>41</sup> and WinGX<sup>42</sup>. The absorption correction was carried out using STOEX-RED and STOEX-SHAPE. All non-hydrogen atoms were calculated anisotropically. The hydrogen atoms were calculated geometrically, and a riding model was applied during the refinement process. Diamond 3.1 was used to draw the crystal structure. For powder XRD analysis, a STOE-STADI MP diffractometer operating in the reflection mode in Bragg-Brentano geometry using Mo-K $\alpha$  ( $\lambda$  = 0.7094 Å) radiation was used. For the analysis of the diffractograms, WinX<sup>POW</sup> was used to identify the corresponding phases. Scanning electron microscopy (SEM) micrographs were recorded on a *Nano SEM 430* with an accelerating voltage of 30 kV. Thermogravimetric measurements were carried out using a TGA/DSC1-STARe-System from METTLER-TOLEDO with a GC100 gas flow controller. The samples were measured under inert conditions in alumina

cuvettes (HEKAtech GmbH, 5-12 mm) until 600 °C or using an aluminum oxide pan up to 1100 °C with a constant heating rate of 10 K/min and a nitrogen flow of 25 ml/min. UV-Vis absorption spectra were recorded with a Varian Cary50 Scan spectrophotometer. The mass spectra were recorded on a Finnigan MAT 95 (EI, 70 eV) in m/z (intensity in %). XAS measurements were carried out in total electron yield mode at the soft X-ray undulator beamline UE56/1-SGM at the synchrotron facility BESSY II, Helmholtz-Zentrum Berlin. Spectra were normalized by background subtraction to 455 and 525 eV and subsequent normalization to unity at 480 and 580 eV for the Ti-L<sub>32</sub>- and O-K-Edges, respectively.

#### ASSOCIATED CONTENT

# **Supporting Information.**

Figure S1: XRD from anatase film formation, using Ti(O<sup>i</sup>Pr)<sub>4</sub> in parallel and perpendicular magnetic fields

Figure S2: SEM images of TiO2 films formed using Ti(OiPr)4 precursor through mfCVD in a) zero-field, b) perpendicular magnetic field orientation.

Figure S3: Numbering scheme for the structure of complex 1.

Table S1. Selected bond lengths [Å] and angles [°] for complex 1.

Figure S4. Crystal structure of complex 1 from single crystal XRD, viewed along the crystallographic a axis, H atoms omitted for clarity.

Table S2. Crystal data and structure refinement for complex 1

# **AUTHOR INFORMATION**

# **Corresponding Author**

\* sanjay.mathur@uni-koeln.de

# **Author Contributions**

The manuscript was written through contributions of all authors. All authors have given approval to the final version of the manuscript.

# **Funding Sources**

- University of Cologne
- Juelich Joint Redox Lab (JJRL).
- German Science Foundation (DFG): "Manipulation of matter controlled by electric and magnetic field: Towards novel synthesis and processing routes of inorganic materials" (SPP 1959).
- Evangelisches Studienwerk Villigst e. V.

# ACKNOWLEDGMENT

The authors gratefully acknowledge the University of Cologne for providing the infrastructure and the German Science Foundation (DFG) for financial support in the frame of the priority program "Manipulation of matter controlled by electric and magnetic field: Towards novel synthesis and processing routes of inorganic materials" (SPP 1959). Daniel Stadler gratefully acknowledges financial support of the Evangelisches Studienwerk Villigst e. V. David N. Mueller gratefully acknowledges support by the Juelich Joint Redox Lab (JJRL). We thank HZB for the allocation of synchrotron radiation beamtime.

# REFERENCES

- (1) Wang, J.; Wang, Z.; Wang, W.; Wang, Y.; Hu, X.; Liu, J.; Gong, X.; Miao, W.; Ding, L.; Li, X.; Tang, J., Synthesis, modification and application of titanium dioxide nanoparticles: a review. *Nanoscale* **2022**, *14* (18), 6709-6734.
- (2) Fagan, R.; McCormack, D. E.; Dionysiou, D. D.; Pillai, S. C. A Review of Solar and Visible Light Active TiO<sub>2</sub> Photocatalysis for Treating Bacteria, Cyanotoxins and Contaminants of Emerging Concern. *Mater. Sci. Semicond. Process.* **2016**, *42*, 2–14.
- (3) Li, Z.; Yao, Z.; Haidry, A. A.; Plecenik, T.; Xie, L.; Sun, L.; Fatima, Q. Resistive-Type Hydrogen Gas Sensor Based on TiO<sub>2</sub>: A Review. *Int. J. Hydrog. Energy* **2018**, *43* (45), 21114–21132.
- (4) Gonçalves, R. A.; Toledo, R. P.; Joshi, N.; Berengue, O. M. Green Synthesis and Applications of ZnO and TiO<sub>2</sub> Nanostructures. *Molecules* **2021**, *26* (8), 2236.
- (5) Li, D.; Bulou, S.; Gautier, N.; Elisabeth, S.; Goullet, A.; Richard-Plouet, M.; Choquet, P.; Granier, A. Nanostructure and Photocatalytic Properties of TiO<sub>2</sub> Films Deposited at Low Temperature by Pulsed PECVD. *Appl. Surf. Sci.* **2019**, *466*, 63–69.
- (6) Dunnill, C. W.; Kafizas, A.; Parkin, I. P. CVD Production of Doped Titanium Dioxide Thin Films. *Chem. Vap. Depos.* **2012**, *18* (4–6), 89–101.
- (7) Vahl, A.; Veziroglu, S.; Henkel, B.; Strunskus, T.; Polonskyi, O.; Aktas, O. C.; Faupel, F. Pathways to Tailor Photocatalytic Performance of TiO<sub>2</sub> Thin Films Deposited by Reactive Magnetron Sputtering. *Materials* **2019**, *12* (17), 2840.
- (8) Niemelä, J.-P.; Marin, G.; Karppinen, M. Titanium Dioxide Thin Films by Atomic Layer Deposition: A Review. *Semicond. Sci. Technol.* **2017**, *32* (9), 093005.

- (9) Huang, J.; Xu, J.; Che, X.; Huang, C. Dismutation of Titanium Sub-oxide into TiO and TiO<sub>2</sub> with Structural Hierarchy Assisted by Ammonium Halides. *Chem. Eur. J.* **2019**, 25 (45), 10642–10649.
- (10) Hagadorn, J. R.; Arnold, J. Titanium(II), -(III), and -(IV) Complexes Supported by Benzamidinate Ligands. *Organometallics* **1998**, *17* (7), 1355–1368.
- (11) Hagadorn, J. R.; Arnold, J. Low-Valent Chemistry of Titanium Benzamidinates Leading to New Ti μ-N <sub>2</sub> , μ-O, Alkyl Derivatives, and the Cyclometalation of TMEDA. *J. Am. Chem. Soc.* **1996**, *118* (4), 893–894.
- (12) McGuinness, D. S.; Gibson, V. C.; Steed, J. W. Bis(Carbene)Pyridine Complexes of the Early to Middle Transition Metals: Survey of Ethylene Oligomerization and Polymerization Capability. *Organometallics* **2004**, *23* (26), 6288–6292.
- (13) Niehues, M.; Erker, G.; Kehr, G.; Schwab, P.; Fröhlich, R.; Blacque, O.; Berke, H. Synthesis and Structural Features of Arduengo Carbene Complexes of Group 4 Metallocene Cations. *Organometallics* **2002**, *21* (14), 2905–2911.
- (14) Jones, N. A.; Liddle, S. T.; Wilson, C.; Arnold, P. L. Titanium(III) Alkoxy-N-Heterocyclic Carbenes and a Safe, Low-Cost Route to TiCl<sub>3</sub> (THF)<sub>3</sub>. *Organometallics* **2007**, *26* (3), 755–757.
- (15) Brown, A. C.; Altman, A. B.; Lohrey, T. D.; Hohloch, S.; Arnold, J. Hydride Oxidation from a Titanium–Aluminum Bimetallic Complex: Insertion, Thermal and Electrochemical Reactivity. *Chem. Sci.* **2017**, 8 (7), 5153–5160.
- (16) Rao, G.; Altman, A. B.; Brown, A. C.; Tao, L.; Stich, T. A.; Arnold, J.; Britt, R. D. Metal Bonding with 3d and 6d Orbitals: An EPR and ENDOR Spectroscopic Investigation of Ti<sup>3+</sup> –Al and Th<sup>3+</sup> –Al Heterobimetallic Complexes. *Inorg. Chem.* **2019**, *58* (12), 7978–7988.
- (17) Giebelhaus, I.; Varechkina, E.; Fischer, T.; Rumyantseva, M.; Ivanov, V.; Gaskov, A.; Morante, J. R.; Arbiol, J.; Tyrra, W.; Mathur, S. One-Dimensional CuO–SnO<sub>2</sub> p–n Heterojunctions for Enhanced Detection of H2S. *J. Mater. Chem. A* **2013**, *1* (37), 11261.
- (18) Jamil, A.; Schlaefer, J.; Goenuellue, Y.; Lepcha, A.; Mathur, S. Precursor-Derived Rare Earth Metal Pyrochlores: Nd<sub>2</sub>Sn<sub>2</sub>O<sub>7</sub> Nanofibers and Thin Films As Efficient Photoabsorbers. *Cryst. Growth Des.* **2016**, *16* (9), 5260–5267.
- (19) Appel, L.; Leduc, J.; Webster, C. L.; Ziller, J. W.; Evans, W. J.; Mathur, S. Synthesis of Air-Stable, Volatile Uranium(IV) and (VI) Compounds and Their Gas-Phase Conversion To Uranium Oxide Films. *Angew. Chem. Int. Ed.* **2015**, *54* (7), 2209–2213.
- (20) Frank, M.; Jürgensen, L.; Leduc, J.; Stadler, D.; Graf, D.; Gessner, I.; Zajusch, F.; Fischer, T.; Rose, M.-A.; Mueller, D. N.; Mathur, S. Volatile Rhenium(I) Compounds with Re–N Bonds and Their Conversion into Oriented Rhenium Nitride Films by Magnetic Field-Assisted Vapor Phase Deposition. *Inorg. Chem.* **2019**, *58* (15), 10408–10416.
- (21) Stadler, D.; Brede, T.; Schwarzbach, D.; Maccari, F.; Fischer, T.; Gutfleisch, O.; Volkert, C. A.; Mathur, S. Anisotropy Control in Magnetic Nanostructures through Field-Assisted Chemical Vapor Deposition. *Nanoscale Adv.* **2019**, *1* (11), 4290–4295.

- (22) Stadler, D.; Mueller, D. N.; Brede, T.; Duchon, T.; Fischer, T.; Sarkar, A.; Giesen, M.; Schneider, C. M.; Volkert, C. A.; Mathur, S. Magnetic Field-Assisted Chemical Vapor Deposition of Iron Oxide Thin Films: Influence of Field-Matter Interactions on Phase Composition and Morphology. *J. Phys. Chem. Lett.* **2019**, *10* (20), 6253–6259.
- (23) Wegner, T.; Petermann, K. Excited State Absorption of Ti<sup>3+</sup>:YAlO<sub>3</sub> *Appl. Phys. B Photophysics Laser Chem.* **1989**, 49 (3), 275–278.
- (24) Petermann, K. The Role of Excited-State Absorption in Tunable Solid-State Lasers. *Opt. Quantum Electron.* **1990**, 22 (S1), S199–S218.
- (25) Barreca, D.; Carraro, G.; Gasparotto, A.; Maccato, C.; Sada, C.; Singh, A. P.; Mathur, S.; Mettenbörger, A.; Bontempi, E.; Depero, L. E. Columnar Fe<sub>2</sub>O<sub>3</sub> Arrays via Plasma-Enhanced Growth: Interplay of Fluorine Substitution and Photoelectrochemical Properties. *Int. J. Hydrog. Energy* **2013**, *38* (33), 14189–14199.
- (26) Mettenbörger, A.; Singh, T.; Singh, A. P.; Järvi, T. T.; Moseler, M.; Valldor, M.; Mathur, S. Plasma-Chemical Reduction of Iron Oxide Photoanodes for Efficient Solar Hydrogen Production. *Int. J. Hydrog. Energy* **2014**, *39* (10), 4828–4835.
- (27) Romero, L.; Piccirillo, C.; Castro, P. M. L.; Bowman, C.; Warwick, M. E. A.; Binions, R. Titanium Dioxide Thin Films Deposited by Electric Field-Assisted CVD: Effect on Antimicrobial and Photocatalytic Properties\*\*. *Chem. Vap. Depos.* **2015**, *21* (1-2–3), 63–70.
- (28) Naik, A. J. T.; Bowman, C.; Panjwani, N.; Warwick, M. E. A.; Binions, R. Electric Field Assisted Aerosol Assisted Chemical Vapour Deposition of Nanostructured Metal Oxide Thin Films. *Thin Solid Films* **2013**, *544*, 452–456.
- (29) Panjawi, N.; Naik, A.; Warwick, M. E. A.; Hyett, G.; Binions, R. The Preparation of Titanium Dioxide Gas Sensors by the Electric Field Assisted Aerosol CVD Reaction of Titanium Isopropoxide in Toluene. *Chem. Vap. Depos.* **2012**, *18* (4–6), 102–106.
- (30) Romero, L.; Binions, R. Effect of AC Electric Fields on the Aerosol Assisted Chemical Vapour Deposition Growth of Titanium Dioxide Thin Films. *Surf. Coat. Technol.* **2013**, *230*, 196–201.
- (31) Laskowski, R.; Blaha, P. Understanding the L 2, 3 x-Ray Absorption Spectra of Early 3d Transition Elements. *Phys. Rev. B* **2010**, 82 (20), 205104.
- (32) Krüger, P. Multichannel Multiple Scattering Calculation of  $L_{2,3}$ -edge Spectra of TiO<sub>2</sub> and SrTiO<sub>3</sub>: Importance of Multiplet Coupling and Band Structure. *Phys. Rev. B* **2010**, 81 (12), 125121.
- (33) Chen, S. C.; Sung, K. Y.; Tzeng, W. Y.; Wu, K. H.; Juang, J. Y.; Uen, T. M.; Luo, C. W.; Lin, J.-Y.; Kobayashi, T.; Kuo, H. C. Microstructure and Magnetic Properties of Oxidized Titanium Nitride Thin Films *in Situ* Grown by Pulsed Laser Deposition. *J. Phys. Appl. Phys.* **2013**, 46 (7), 075002.
- (34) Wang, D.; Liu, L.; Sun, X.; Sham, T.-K. Observation of Lithiation-Induced Structural Variations in TiO<sub>2</sub> Nanotube Arrays by X-Ray Absorption Fine Structure. *J. Mater. Chem. A* **2015**,

- *3* (1), 412–419.
- (35) Mo, L.-B.; Bai, Y.; Xiang, Q.-Y.; Li, Q.; Wang, J.-O.; Ibrahim, K.; Cao, J.-L. Band Gap Engineering of TiO<sub>2</sub> through Hydrogenation. *Appl. Phys. Lett.* **2014**, *105* (20), 202114.
- (36) Lepcha, A.; Maccato, C.; Mettenboerger, A.; Andreu, T.; Mayrhofer, L.; Walter, M.; Olthof, S.; Ruoko, T.-P.; Klein, A.; Moseler, M.; Meerholz, K.; Morante, J. R.; Barreca, D.; Mathur, S. Electrospun Black Titania Nanofibers: Influence of Hydrogen Plasma-Induced Disorder on the Electronic Structure and Photoelectrochemical Performance. *J. Phys. Chem. C* **2015**, *119* (33), 18835–18842.
- (37) Singh, T.; Müller, R.; Singh, J.; Mathur, S. Tailoring Surface States in WO<sub>3</sub> Photoanodes for Efficient Photoelectrochemical Water Splitting. *Appl. Surf. Sci.* **2015**, *347*, 448–453.
- (38) Shondo, J.; Veziroglu, S.; Tjardts, T.; Sarwar, T. B.; Mishra, Y. K.; Faupel, F.; Aktas, O. C. Nanoscale Synergetic Effects on Ag–TiO<sub>2</sub> Hybrid Substrate for Photoinduced Enhanced Raman Spectroscopy (PIERS) with Ultra-Sensitivity and Reusability. *Small* **2022**, *18* (50), 2203861.
- (39) Sheldrick, G. M. A Short History of SHELX. Acta Crystallogr. A 2008, 64 (1), 112–122.
- (40) Altomare, A.; Cascarano, G.; Giacovazzo, C.; Guagliardi, A.; Burla, M. C.; Polidori, G.; Camalli, M. *SIR* 92 a Program for Automatic Solution of Crystal Structures by Direct Methods. *J. Appl. Crystallogr.* **1994**, *27* (3), 435–435.
- (41) Sheldrick, G. M. Crystal Structure Refinement with *SHELXL*. *Acta Crystallogr*. *Sect. C Struct*. *Chem.* **2015**, *71* (1), 3–8.
- (42) Farrugia, L. J. WinGX and ORTEP for Windows: An Update. J. Appl. Crystallogr. **2012**, 45 (4), 849–854.